Nanostructured Spintronic Emitters for Polarization-Textured and Chiral Broadband THz Fields

Dominik Schulz,* Benjamin Schwager, and Jamal Berakdar

ACCESS | Metrics & More | Article Recommendations | Supporting Information

ABSTRACT: Spintronic THz emitters (STEs) rely on spin current acceleration or decay, resulting in a burst of broadband THz emission, offering a new route to THz optics. Here, we demonstrate novel metastructures of STEs for molding the vectorial focal distribution of the emitted THz radiations. The metastructures also allow controlling the characteristics of local fields. Performing combined micromagnetic-electromagnetic simulations, we demonstrate the generation of broadband THz fields with designed vectorial, chiral, magnetic, or topological features and discuss the potential of these fields for studying magnetic, multiferroic, and chiral structures. The STEs metastructure is shown to produce higher-order electric and magnetic multipoles as well as localized, longitudinal, broadband magnetoelectric THz pulses. Furthermore, subwavelength features of the near fields at a distance less than 10 μm can be tuned by steering the

magnetization of the metastructure. The results point to a new type of engineered STEs for the generation of structured broadband THz fields, with potential applications in the fields of optoelectronics, optics, and ultrafast magnetism.

KEYWORDS: *THz sources, vector beams, spintronic THz emitters, metastructure, chiral fields, magnetoelectric interaction*
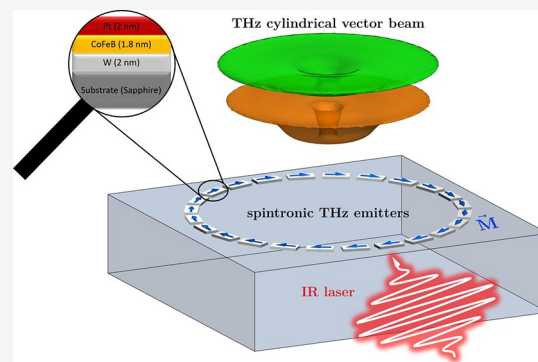
1. INTRODUCTION

Electromagnetic THz radiation has a variety of important applications ranging from fundamental science to imaging and information technology.[1,2] In conventional THz emitters, an infrared pump pulse triggers a swiftly decaying charge current in a nonlinear or a photoconductive medium, resulting in free-space coherent THz radiation.[1] Recently, so-called spintronic terahertz emitters (STEs) have been demonstrated. The STE, in its basic realization (as schematically shown in Figure 1), consists of a ferromagnet (FM) interfaced with a thin nonmagnetic layer (NM) with strong spin−orbit coupling.[3−5]

Irradiating the STE with a femtosecond infrared (IR) laser pulse generates a nonequilibrium charge distribution accompanied by a diffusive longitudinal spin-polarized current because the mobilities of the spin-up and spin-down electrons in the FM are different. When traversing the NM layer, this spin current leads to a transversal charge current due to the inverse spin Hall effect. The charge current decays on the subpicosecond time scale leading to THz emission. The charge current direction is perpendicular to the spin-current and the magnetization directions.[6−14]

In this work, we focus on the application of STEs for the generation of broadband THz pulses with engineered spatiotemporal characteristics. In particular, we consider broadband THz cylindrical vector beams (VBs), meaning propagating THz fields with radial, azimuthal, or chiral polarization textures. Current methods for generating VBs

include photoconductive antennas,[15−18] mode conversion,[19] and velocity-mismatched optical rectification[20] (for further methods, we refer to refs 21−24). VBs are useful for optoelectronic and optospintronic applications,[25−28] since various elementary excitations are in the THz range. Broadband THz pulses can drive directed currents[29] or excitations caused by the electric and magnetic longitudinal field components.[30,31] Other promising applications include optical tweezers and trapping,[32] molecular orientation control,[33] particle acceleration,[34] and fluorescence microscopy.[35]

To produce structured electromagnetic fields, the vectorial and spatial phase properties have to be shaped. The novel approach presented here is based on exploiting the intrinsic magnetic interactions that determine the magnetization direction in a finite-size STE and engineering several separated STEs into a metastructure to produce a desired spatial magnetization profile $\mathbf{M}(\mathbf{r})$. In turn, $\mathbf{M}(\mathbf{r})$ sets the local direction of the charge-current density that generates the broadband THz fields with a polarization depending thus on

1248

https://doi.org/10.1021/acsphotonics.1c01693
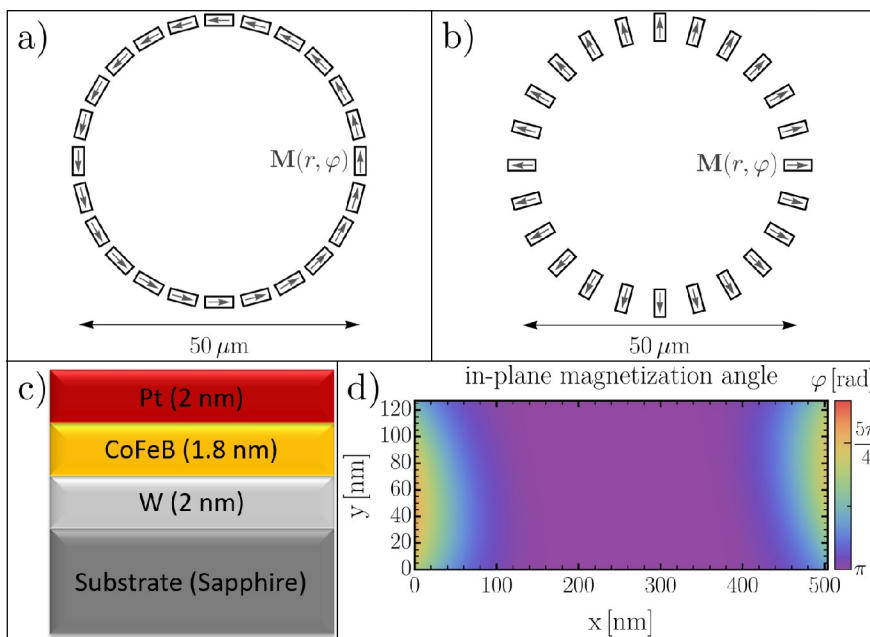*ACS Photonics* 2022, 9, 1248−1255
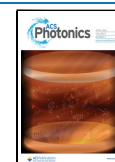
Figure 1. STEs metastructures for generating broadband THz vector beams. STEs metastructure leading to (a) radially or (b) azimuthally polarized broadband THz radiation. (c) Cross section of an individual STE comprising a nanoscale Pt layer deposited on a ferromagnetic $Co_{20}Fe_{60}B_{20}$ film followed by a W layer and all deposited on a sapphire substrate. (d) Spatial profile of the ground state magnetization of a single STE (with dimension $(128 \times 512 \times 1.8)$ nm^3), as determined by an intrinsic interaction as well as with dipolar fields due to neighboring STEs. The temperature is $T = 298$ K. The arrows on the STEs indicate the calculated direction of the ground state magnetization.

$\mathbf{M(r)}/|\mathbf{M(r)}|$. In this way, the vectorial and focal feature of the THz radiation can be tuned on a submicron scale. The concept is validated by performing combined micromagnetic and electromagnetic simulations. We show that the STEs metastructures emit broadband THz fields with radial or azimuthal polarization or chiral fields with structured spin-angular momentum (SAM) densities. We note that for narrowband coherent fields, the control of chirality, SAM, and orbital angular momentum can be achieved by several methods that include spatial light modulators,[36] spiral phase plates or mirrors,[37,38] liquid crystals (q-plate),[39] subwavelength gratings with dielectric grooves,[40] metasurfaces (spatially varying optical response) based on anomalous reflection and refraction phenomena,[41,42] besides silicon-based Huygens' dielectric metasurfaces, and J-plates.[43−45] STEs are, however, broadband emitters due to the intrinsically diffusive and damped nature of the charge current density (due to Ohmic losses).

The work is organized as follows. Section 2 provides details on the materials and working principle of the STEs metastructure. Section 3 contains the analysis of the temporal, spectral, and polarization features of the THz fields. Section 4 presents a scheme for chiral THz fields generation and discusses possible applications of the emitted fields.

2. ENGINEERED SPINTRONIC THZ EMITTERS

We study STEs consisting of magnetized $Co_{20}Fe_{60}B_{20}$ (CoFeB) as the FM, and Pt and W as the normal metal (NM) spin−orbit scatterer (details of their optical properties are discussed in ref 46). The concept and general results are independent of the specific material, however. The metastructures (Figure 1a,b) consist of air-separated individual STEs (Figure 1c) deposited on a substrate. For one STE, the CoFeB layer thickness is 1.8 nm, and that of Pt is 2 nm. The W

layer thickness is 2 nm, and the sapphire substrate thickness is larger than 50 μm.

As specific examples for generating structured broadband, THz fields, we consider the schemes in Figure 1a,b as the basic building units that can be repeated as well-separated concentric (or stacked) rings to enhance the emitted power without compromising the qualitative features of the fields in the center of the structure. An essential property of the operation principle is the spatial distribution of the ground state magnetic ordering $\mathbf{M(r)}$, which is determined by intrinsic interactions within the individual STEs such as exchange interaction, magnetic anisotropies, and demagnetization fields, as well as by the dipolar interactions between the STEs. We infer the ground state from full-numerical micromagnetic simulations based on the Landau−Lifshitz−Gilbert equation (technical details are provided in the Supporting Information, SI). Our scheme exploits the effect of the shape anisotropy, which leads to a spatial dependence of $\mathbf{M(r)}$ on the geometric shape of a nanostructure (the STE in our case). $\mathbf{M(r)}$ within an individual STE is determined by magnetic interactions within the STE as well as by the dipolar fields due to the next neighboring STEs. An example is shown in Figure 1d. $\mathbf{M(r)}$ is basically homogeneous, except for small variations at the boundaries. The reason is that the radius of the metastructure is much larger than the dimensions of a single STE. And the STEs are well separated (as to make use of the shape anisotropy and suppress inter-STEs dipolar fields). The established ground state magnetization profile of the metastructures is indicated by the arrows in Figure 1a,b.

Starting from the magnetic ground state inferred from the simulations, we assume the metastructure is irradiated by an IR laser with an electric field $\mathbf{E}_{IR}$. Previous studies in refs 3−5 established an experimentally verified model for how $\mathbf{E}_{IR}$ interacts with a single STE, leading to the generation of a directed charge current density $\mathbf{j}_c$ (due to spin diffusion of hot
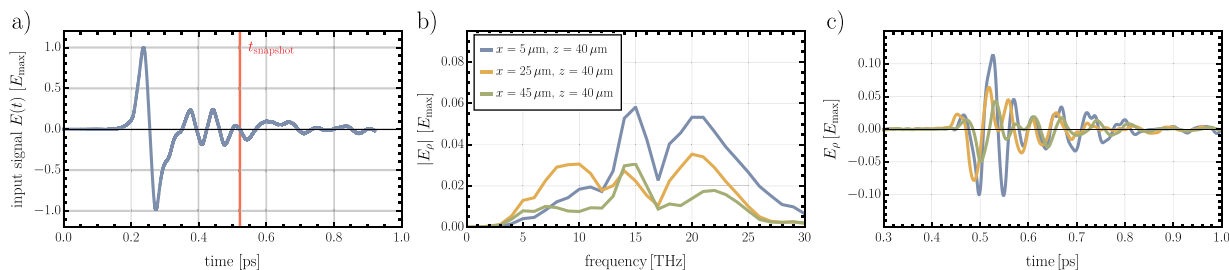
Figure 2. Local temporal and spectral features of STEs-generated fields. (a) The experimentally reported (ref 4) input signal applied to the STEs in the metastructure. E_{max} denotes the peak field. The red line indicates the time at which Figures 3 and 4 are evaluated. The frequency (b) and the time (c) dependencies of the beam produced by the pattern in Figure 1a with 24 STEs in the plane across the beam at the indicated vertical distance z from the metastructure center ($x = 0$, $y = 0$, $z = 0$). In (b) and (c), $y = 0$.
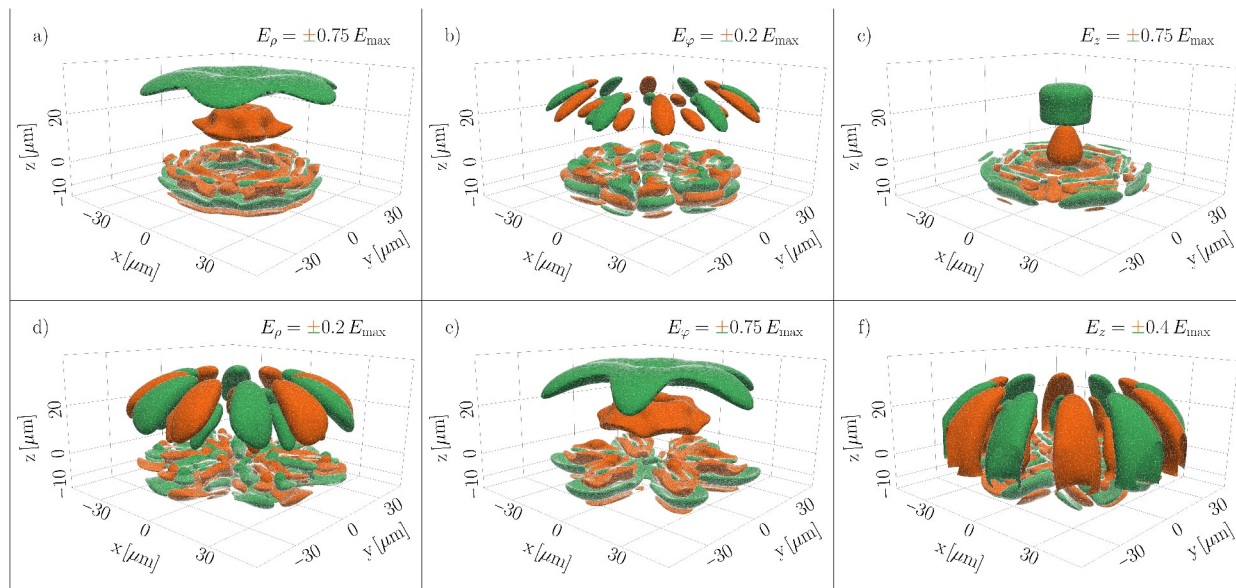

Figure 3. Field distributions emitted by STEs-metastructures. The fields components $E_{\rho,\varphi,z}$ in cylindrical coordinates are shown as contour plots and display the spatial, temporal, and vectorial properties of the THz emission. Variations from green to orange color indicate the change from positive to negative polarity of the field while propagating along the z-axis. Field emitted from the metastructure in Figure 1a are in insets (a)−(c), and those from the structure in Figure 1b are in insets (d)−(f). The metastructures consisting of six STEs define the x−y plane. All snapshots are taken at the time 0.53 ps.

carriers and inverse spin Hall effect). It is shown experimentally and theoretically that j_c is relatively weak such that j_c can be related linearly to a local electric field E_0. Henceforth, we adopt this model. The direction of E_0 is orthogonal to $M(r)$. The time structure of E_0 follows that of j_c.

For evaluating the experimental feasibility of our scheme, we use for the simulations presented here the time profile of E_0, the one determined by experiment,[4] and transform it into the frequency domain, where the calculations are performed (compare Figure 2a; any other profile can be adopted). Current experiments achieve a peak electric field of $E_{max} \sim 300$ kV/cm.[4]

Starting with E_0, we performed electromagnetic simulations and obtained the field distributions in the time and the frequency domains (full technical details are in SI).

3. ANALYSIS OF THE RADIATED FIELDS

3.1. Temporal and Spectral Features.
Solving the Maxwell equations in the frequency domain, we obtain the spectral content of the beams as well as the local temporal evolution. Both the spectral and temporal aspects depend on the distance along the beam axis and vary across the beam.

Figure 2 shows typical results for the fields emitted from the metastructure shown by Figure 1a with 24 STEs. During the propagation, the fields emanating from individual emitters interfere so that certain frequencies are suppressed or enhanced (cf. Figure 2b). This effect is most pronounced in the vicinity of the beam axis. The time signal reflects this behavior with a delay concerning the input field set by the propagation time (cf. Figure 2c).

3.2. Polarization Textures.
Figures 3 and 4 show the simulation results for the fields' spatial distributions radiated by the metastructure in Figure 1a or b. The qualitative features are only weakly dependent on frequency, and hence, we confine the discussion to one frequency. The propagating fields are fully formed after a few microns along the z-axis. All field components possess discrete rotational symmetry with respect to the z-axis. The number of emitters determines the symmetry order.

Figures 3 and 4 display the radial (E_ρ), azimuthal (E_φ), and longitudinal (E_z) components of the emitted electric fields for metastructures having 6 or 24 STEs (with the same radius). Figure 3a−c corresponds to the metastructure in Figure 1a, while Figure 3d−f corresponds to that in Figure 1b.
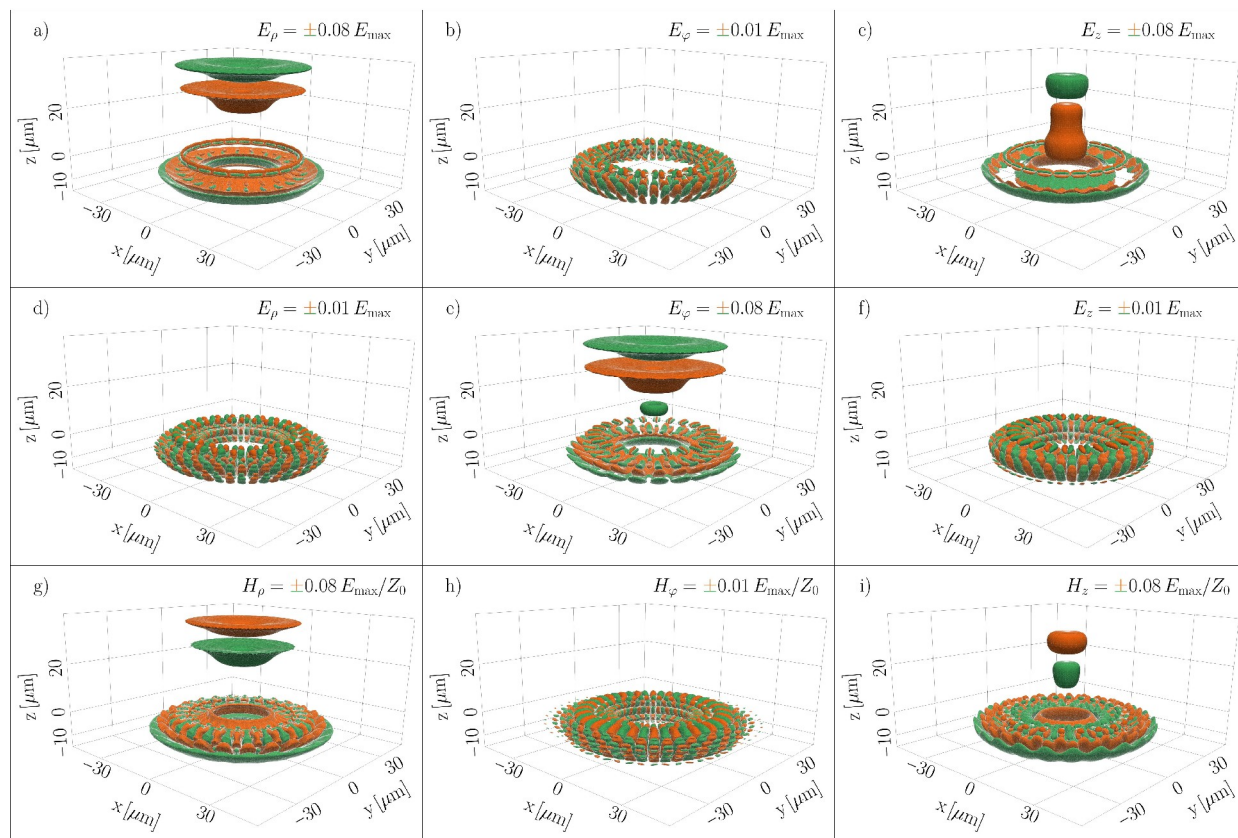
Figure 4. Spatial field distributions radiated by dense STEs-metastructure. Distributions of the electric fields generated by 24 STEs ordered in the metastructure in Figure 1a (insets a−c) or Figure 1b (insets d−f). The metastructure defines the $x-y$ plane. All snapshots are taken at the time 0.53 ps. Insets (g)−(i) show the magnetic field distributions for the metastructure in Figure 1b. Other parameters, notations, and color coding are the same as those in Figure 3.

Figure 3a−c is evidence that the metastructure in Figure 1a generates propagating fields with dominant radial and longitudinal components, while Figure 1b yields THz radiation with a dominant azimuthal component. Thus, we conclude that the metastructure in Figure 1a or b yields, respectively, predominantly radially or azimuthally polarized beams.

To make this observation more quantitative, we consider at first analytically the free-space VB solutions of the Maxwell-equations with radial and azimuthal polarization and categorize a beam according to its electric and magnetic multipoles (details are in SI): Radially (azimuthally) polarized VB contains only electric (magnetic) multipoles. Then, we expand our simulation results for the propagating part of the fields in vector spherical harmonics and obtain the multipole content of the fields for a particular metastructure numerically (see SI). In this way, we are able to specify the type of the generated field as well as its quality (judged by the distribution of the contributing multipoles). It is found that the order of the multipoles is related to the number of STEs. The multipole analysis confirms that the metastructure in Figure 1a or b radiates radially or azimuthally polarized VBs with the quality being enhanced with an increasing number of STEs (at a fixed radius of the ring).

The near fields in the immediate vicinity of the emitter are dictated by the individual STE hosting the local current-density distribution. Interference sets in at a distance comparable to the separation length between the STEs, in which case, the global geometry/topology of the metastructure starts to affect the structure of the field. Comparing Figure 3

and Figure 4, we conclude that, with an increased number of STEs, the propagating parts separate from the local fields at a smaller distance and become more focused, meaning the vectorial properties (in terms of radial or azimuthal polarization) become well-defined. Figure 4g−i also evidence the relevance of the STEs structure for magnetic applications. The THz magnetic field can be collimated to a region around the propagation direction well below the metastructure size (cf. Figure 4i).

4. CHIRAL FIELD GENERATION AND INTERACTION WITH MATTER

The STEs metastructures, Figure 1a,b, are capable of generating radially and azimuthally polarized THz fields. This does not mean that these fields embody a finite chirality-density,[47] C. In fact, for an electromagnetic field oscillating with the angular frequency ω, the time-averaged C is given by[47]

$$C = \frac{\omega}{2c^2} \Im\{\mathbf{E} \cdot \mathbf{H}^*\}. \tag{1}$$

Thus, $C \neq 0$ implies a finite amplitude of the components E_z and H_z of the electric and magnetic fields and also a finite phase difference between them. Purely radially or azimuthally polarized vector beams, such as those shown in Figures 4, have vanishing chirality-density (electric and magnetic field components are mutually orthogonal). A field with a finite C is desirable for studying chiral matter. The exchange of C
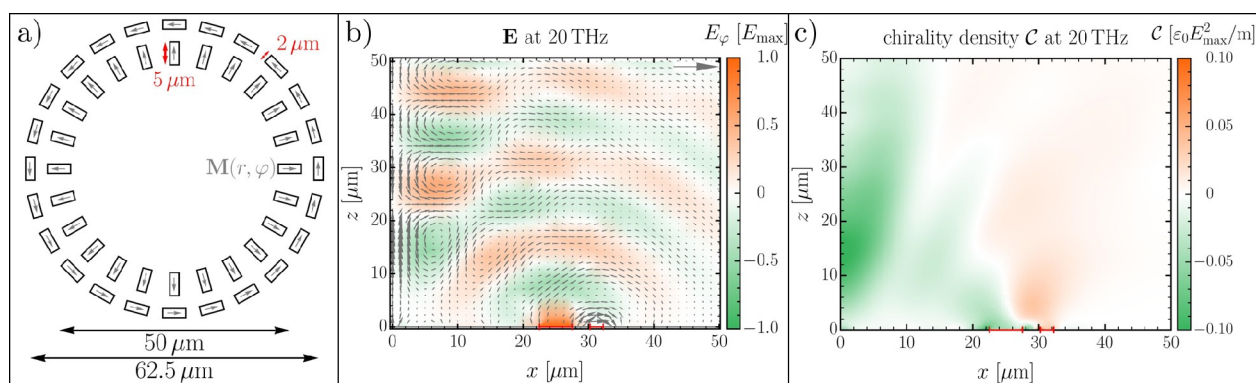
Figure 5. Metastructure, field distribution, and the chirality-density of the field. (a) Metastructure as a combination of Figure 1a,b for generating chiral broadband THz fields. (b) Electric field distribution at a frequency of 20 THz. The arrow in the top right corner indicates the unit vector length. The position and width of the STE are indicated by red bars at the x-axis. (c) The spatial distribution of the time-averaged chirality density at the same frequency.

between fields and sources (in the absence of currents) is governed by the continuity equation

$$\partial_t C + \nabla \cdot \mathbf{F}_C = 0 \tag{2}$$

with $\mathbf{F}_C$ denoting the chirality flux-density. For the special case of harmonic fields within a source-free space, $\mathbf{F}_C$ is proportional to the spin angular momentum density[48,49] given by

$$\mathbf{S} = \frac{1}{4\omega} \mathfrak{I}\{\varepsilon \mathbf{E}^* \times \mathbf{E} + \mu \mathbf{H}^* \times \mathbf{H}\} \tag{3}$$

$\mathbf{S}$ is of a key importance for trapping and spinning of particles.[50]

4.1. STE Metastructures for Chiral Field Generation. A hint on which metastructures generate THz fields with finite chirality is inferred from Figure 4c and i, for which, respectively, $|E_z|$ and $|H_z|$ are finite. Thus, enclosing the metastructure in Figure 1a within that in Figure 1b should produce fields with finite electric and magnetic z-components with strong localization around the z-axis.

For the metastructure in Figure 5(a) (we ensured that the depicted arrows correspond to the ground state magnetization), we calculated the emitted THz fields (Figure 5b). The Figure 5b indicates that the electric field amplitude is maximal within a narrow region around the z-axis. The longitudinal component is dominant. The same applies to the magnetic field. As the field multipole expansion is linear, we can expect that the structure in Figure 5 generates fields with sizable electric and magnetic multipoles with the intensity being focused around the propagation direction. The strongly localized nature of the z-components of the electric and the magnetic fields around the z-axis is reflected in sizable chirality-density near the optical axis. The required phase lag between $|E_z|$ and $|H_z|$ (cf. eq 1) is brought about by the different radii of the angularly and radially magnetized ring structures in Figure 5a. The precise position along the optical axis where the time-averaged chirality-density is maximal depends on the frequency of the field (because of the key role of interference). The maximum of $C(\omega)$ correlates with the axial distance from the emitter, which may be useful for spectroscopic investigations.

4.2. Interaction of the Emitted THz Fields with Matter. Being able to generate localized, broadband THz fields with shaped vectorial and chiral properties, the question is how to functionalize these features for material studies. Therefore, we revisit the radiation interaction with matter.

Generally, the free energy F_0 of a system may change to F upon coupling to external electromagnetic fields $\mathbf{E}$, $\mathbf{H}$ as[51]

$$\begin{aligned} F(\mathbf{E}, \mathbf{H}) = \int_V f \ \mathrm{d}V &= F_0(\mathbf{P}_S, \mathbf{M}_S) - \int_V (\mathbf{P}_S \cdot \mathbf{E} + \mu_0 \mathbf{M}_S \cdot \mathbf{H}) \ \mathrm{d}V \\ &- \int_V \mathfrak{R}\{\varepsilon_0 \mathbf{E}^* \chi^e \mathbf{E} + \mu_0 \mathbf{H}^* \chi^m \mathbf{H} + \mathbf{E}^* \alpha \mathbf{H}\} \ \mathrm{d}V \\ &- \int_V O(EH^2, HE^2, E^3, H^3) \ \mathrm{d}V \end{aligned} \tag{4}$$

$\mathbf{P}_S$ and $\mathbf{M}_S$ stand for pre-existing spontaneous ferroelectric polarization and magnetization, and χ^e and χ^m are the material-dependent tensors of electric and magnetic susceptibility, respectively. α is the (necessarily Hermitian) tensor of linear magnetoelectric susceptibility that describes the magnetic (electric) responses to external electric (magnetic) fields. Higher-order responses may contribute but are not considered here. The polarization and magnetization in the presence of the fields follow from

$$P_i = -\frac{\delta f}{\delta E_i}, \quad M_i = -\frac{1}{\mu_0} \frac{\delta f}{\delta H_i}, \quad i \in \{1; 2; 3\} \tag{5}$$

For FM or antiferromagnetic materials, we can study the local magnetic dynamics (and the THz response χ^m) for a sample deposited above the center of the metastructure shown in Figure 1b. This structure produces around the z-axis a strong magnetic field only (cf. Figure 4i). For a ferroelectric material, similar arguments apply for studying the response by using the metastructure Figure 1a (cf. the field in Figure 4c). Linear magnetoelectric samples can be studied by monitoring and comparing the response to the fields generated by Figure 1a or b. The quadratic magnetoelectric response is as well separately accessible $P_i = \gamma_{iii}H_iE_i$: By stacking the metastructures, Figure 1a,b on top of each other, one may produce fields that have strong E_z and H_z components localized around the axis (roughly the sum of fields in Figure 4c(i)), in which case γ_{zzz} can be studied. The quadratic magnetoelectric response is not necessarily chiral. To elaborate on where our chiral fields, shown in Figure 5, may be useful, for example, for enantiomers. We recall that the microscopic electric ($\mathbf{p}$) and magnetic ($\boldsymbol{\mu}$) dipoles induced in response to $\mathbf{E}$ and $\mathbf{H}$ are given by[47]

$$\mathbf{p} = (\varepsilon_0 \chi^e \mathbf{E} - \mathrm{i} g \mathbf{H}) \quad \text{and} \quad \boldsymbol{\mu} = \left(\chi^m \mathbf{H} + \mathrm{i} \frac{g}{\mu_0} \mathbf{E}\right) \tag{6}$$

with g being a coupling constant. The contribution to the free energy-density f depends on the chirality-density of the

external fields because it contains the term $\frac{\mathrm{i}}{2}g(\mathbf{E}^* \cdot \mathbf{H} - \mathbf{H}^* \cdot \mathbf{E}) = g\mathfrak{I}\{\mathbf{H}^* \cdot \mathbf{E}\} \propto C$. Variations in C of our THz fields (for instance, its sign) allows for sensing of the chiral content in the sample (via monitoring the response in $\mathbf{p}$ and $\boldsymbol{\mu}$), similarly as discussed in refs 47, 52, and 53. Also, the spatial structure of $C = C(\mathbf{r}, t)$ of our fields (shown in Figure 2c) can be exploited for chiral spectroscopy with spatiotemporal resolution which is particularly useful for spatial distributions of nanoscopic chiral structures or molecules for which $g = g(\mathbf{r})$.

Notably, our metastructures focus and structure the intensity profile and the vectorial properties on the submicrometer scale (cf. Figure 4,2). This allows studying materials with anisotropic electric and magnetic susceptibilities, which for instance, has the form

$$\chi_{jk}^{\mathrm{e}} = (\varepsilon_{\mathrm{r}} - 1)\delta_{jk} + i\bar{f}\,\epsilon_{\alpha jk} \text{ and } \chi_{jk}^{\mathrm{m}} = (\mu_{\mathrm{r}} - 1)\delta_{jk} + i\bar{f}\,\epsilon_{\alpha jk} \tag{7}$$

$\varepsilon_{\alpha jk}$ is the Levi-Civita symbol, and $\bar{f}$ is a real constant. Inserting eq 7 in F and recalling that F is a scalar, we conclude that the anisotropic responses imply a distinct dependence on fields of the form $\mathfrak{I}(\mathbf{E}^* \times \mathbf{E})_\alpha$ or $\mathfrak{I}(\mathbf{H}^* \times \mathbf{H})_\alpha$, having a component-by-component proportionality to the SAM-density (not shown for brevity, but can be inferred from Figure 5 and eqs 1, 4, and 3). We recall that, in the IR and XUV regimes, SAM textured fields have already been demonstrated, for instance, in refs 54−57, and the present proposal allows extending such studies to the THz regime.

5. CONCLUSIONS

We introduced a novel, STEs-based method for the generation of broadband vector beams in the THz regime. Quantifying the emitted fields via their electric and magnetic multipoles, we evidence the possibility of producing radially or azimuthally polarized broadband THz fields as well as chiral fields with structured spin angular momentum density embodying a finite chirality. By analyzing the coupling of the fields to matter, we pointed out several applications of the generated fields. An extension of the current scheme for strongly miniaturized STE should account for finite-size effects such as possible backward charge current that leads to a lowering of the signal amplitude.[58,59] Also, for dense STEs packing, dipolar interaction may lead to noncollinear magnetic ordering and the mechanism of the charge current generation need to be revisited.

ASSOCIATED CONTENT

Supporting Information

The Supporting Information is available free of charge at https://pubs.acs.org/doi/10.1021/acsphotonics.1c01693.

> Micromagnetic simulation details, electromagnetic simulation details, and multipole expansion (PDF)

AUTHOR INFORMATION

Corresponding Author

Dominik Schulz − Institut für Physik, Martin-Luther-Universität Halle-Wittenberg, 06099 Halle, Saale, Germany; orcid.org/0000-0002-0471-1622; Email: dominik.schulz@physik.uni-halle.de

Authors

Benjamin Schwager − Institut für Physik, Martin-Luther-Universität Halle-Wittenberg, 06099 Halle, Saale, Germany

Jamal Berakdar − Institut für Physik, Martin-Luther-Universität Halle-Wittenberg, 06099 Halle, Saale, Germany; orcid.org/0000-0001-8727-3981

Complete contact information is available at:
https://pubs.acs.org/10.1021/acsphotonics.1c01693

Author Contributions

All authors contributed to the performance of the project and to the discussion and writing of the manuscript. Numerical simulations and analysis were done by D.S.

Notes

The authors declare no competing financial interest.

REFERENCES

(1) Mittleman, D. M. Perspective: Terahertz science and technology. *J. Appl. Phys.* **2017**, *122*, 230901.

(2) Tonouchi, M. Cutting-edge terahertz technology. *Nat. Photonics* **2007**, *1*, 97−105.

(3) Kampfrath, T.; Tanaka, K.; Nelson, K. A. Resonant and nonresonant control over matter and light by intense terahertz transients. *Nat. Photonics* **2013**, *7*, 680−690.

(4) Seifert, T.; et al. Efficient metallic spintronic emitters of ultrabroadband terahertz radiation. *Nat. Photonics* **2016**, *10*, 483−488.

(5) Papaioannou, E. T.; Beigang, R. THz spintronic emitters: a review on achievements and future challenges. *Nanophotonics* **2021**, *10*, 1243−1257.

(6) Jin, Z.; Tkach, A.; Casper, F.; Spetter, V.; Grimm, H.; Thomas, A.; Kampfrath, T.; Bonn, M.; Kläui, M.; Turchinovich, D. Accessing the fundamentals of magnetotransport in metals with terahertz probes. *Nat. Phys.* **2015**, *11*, 761−766.

(7) Battiato, M.; Carva, K.; Oppeneer, P. M. Superdiffusive Spin Transport as a Mechanism of Ultrafast Demagnetization. *Phys. Rev. Lett.* **2010**, *105*, 027203.

(8) Nenno, D. M.; Kaltenborn, S.; Schneider, H. C. Boltzmann transport calculation of collinear spin transport on short timescales. *Phys. Rev. B* **2016**, *94*, 115102.

(9) Alekhin, A.; Razdolski, I.; Ilin, N.; Meyburg, J. P.; Diesing, D.; Roddatis, V.; Rungger, I.; Stamenova, M.; Sanvito, S.; Bovensiepen, U.; Melnikov, A. Femtosecond Spin Current Pulses Generated by the Nonthermal Spin-Dependent Seebeck Effect and Interacting with Ferromagnets in Spin Valves. *Phys. Rev. Lett.* **2017**, *119*, 017202.

(10) Hohlfeld, J.; Wellershoff, S.-S.; Güdde, J.; Conrad, U.; Jähnke, V.; Matthias, E. Electron and lattice dynamics following optical excitation of metals. *Chem. Phys.* **2000**, *251*, 237−258.

(11) Werake, L. K.; Ruzicka, B. A.; Zhao, H. Observation of Intrinsic Inverse Spin Hall Effect. *Phys. Rev. Lett.* **2011**, *106*, 107205.

(12) Hoffmann, A. Spin Hall Effects in Metals. *IEEE Trans. Magn.* **2013**, *49*, 5172−5193.

(13) Wei, D.; Obstbaum, M.; Ribow, M.; Back, C. H.; Woltersdorf, G. Spin Hall voltages from a.c. and d.c. spin currents. *Nat. Commun.* **2014**, *5*, 3768.

(14) Sinova, J.; Valenzuela, S. O.; Wunderlich, J.; Back, C. H.; Jungwirth, T. Spin Hall effects. *Rev. Modern Phys.* **2015**, *87*, 1213−1260.

(15) Deibel, J. A.; Wang, K.; Escarra, M. D.; Mittleman, D. Enhanced coupling of terahertz radiation to cylindrical wire waveguides. *Opt. Express* **2006**, *14*, 279.

(16) Winnerl, S.; Zimmermann, B.; Peter, F.; Schneider, H.; Helm, M. Terahertz Bessel-Gauss beams of radial and azimuthal polarization from microstructured photoconductive antennas. *Opt. Express* **2009**, *17*, 1571.

(17) Winnerl, S.; Hubrich, R.; Mittendorff, M.; Schneider, H.; Helm, M. Universal phase relation between longitudinal and transverse fields observed in focused terahertz beams. *New J. Phys.* **2012**, *14*, 103049.

(18) Cliffe, M. J.; Rodak, A.; Graham, D. M.; Jamison, S. P. Generation of longitudinally polarized terahertz pulses with field amplitudes exceeding 2 kV/cm. *Appl. Phys. Lett.* **2014**, *105*, 191112.

(19) Grosjean, T.; Baida, F.; Adam, R.; Guillet, J.-P.; Billot, L.; Nouvel, P.; Torres, J.; Penarier, A.; Charraut, D.; Chusseau, L. Linear to radial polarization conversion in the THz domain using a passive system. *Opt. Express* **2008**, *16*, 18895.

(20) Chang, G.; Divin, C. J.; Liu, C.-H.; Williamson, S. L.; Galvanauskas, A.; Norris, T. B. Generation of radially polarized terahertz pulses via velocity-mismatched optical rectification. *Opt. Lett.* **2007**, *32*, 433.

(21) Imai, R.; Kanda, N.; Higuchi, T.; Zheng, Z.; Konishi, K.; Kuwata-Gonokami, M. Terahertz vector beam generation using segmented nonlinear optical crystals with threefold rotational symmetry. *Opt. Express* **2012**, *20*, 21896.

(22) Minami, Y.; Kurihara, T.; Yamaguchi, K.; Nakajima, M.; Suemoto, T. Longitudinal terahertz wave generation from an air plasma filament induced by a femtosecond laser. *Appl. Phys. Lett.* **2013**, *102*, 151106.

(23) Zheng, Z.; Kanda, N.; Konishi, K.; Kuwata-Gonokami, M. Efficient coupling of propagating broadband terahertz radial beams to metal wires. *Opt. Express* **2013**, *21*, 10642.

(24) Woldegeorgis, A.; Kurihara, T.; Almassarani, M.; Beleites, B.; Grosse, R.; Ronneberger, F.; Gopal, A. Multi-MV/cm longitudinally polarized terahertz pulses from laser−thin foil interaction. *Optica* **2018**, *5*, 1474.

(25) Wätzel, J.; Granados-Castro, C. M.; Berakdar, J. Magneto-electric response of quantum structures driven by optical vector beams. *Phys. Rev. B* **2019**, *99*, 085425.

(26) Wätzel, J.; Berakdar, J. Centrifugal photovoltaic and photo-galvanic effects driven by structured light. *Sci. Rep.* **2016**, *6*, 21475.

(27) Wätzel, J.; Berakdar, J. All-optical generation and ultrafast tuning of non-linear spin Hall current. *Sci. Rep.* **2018**, *8*, 17102.

(28) Wätzel, J.; Sherman, E. Y.; Berakdar, J. Nanostructures in structured light: Photoinduced spin and orbital electron dynamics. *Phys. Rev. B* **2020**, *101*, 235304.

(29) Moskalenko, A. S.; Zhu, Z.-G.; Berakdar, J. Charge and spin dynamics driven by ultrashort extreme broadband pulses: A theory perspective. *Phys. Rep.* **2017**, *672*, 1−82.

(30) Fujita, H.; Sato, M. Nonequilibrium Magnetic Oscillation with Cylindrical Vector Beams. *Sci. Rep.* **2018**, *8*, 15738.

(31) Fujita, H.; Tada, Y.; Sato, M. Accessing electromagnetic properties of matter with cylindrical vector beams. *New J. Phys.* **2019**, *21*, 073010.

(32) Friedman, N.; Kaplan, A.; Davidson, N. *Advances In Atomic, Molecular, and Optical Physics*; Elsevier, 2002; pp 99−151.

(33) Sick, B.; Hecht, B.; Novotny, L. Orientational Imaging of Single Molecules by Annular Illumination. *Phys. Rev. Lett.* **2000**, *85*, 4482−4485.

(34) Nanni, E. A.; Huang, W. R.; Hong, K.-H.; Ravi, K.; Fallahi, A.; Moriena, G.; Miller, R. J. D.; Kärtner, F. X. Terahertz-driven linear electron acceleration. *Nat. Commun.* **2015**, *6*, 8486.

(35) Watanabe, T.; Iketaki, Y.; Omatsu, T.; Yamamoto, K.; Sakai, M.; Fujii, M. Two-point-separation in super-resolution fluorescence microscope based on up-conversion fluorescence depletion technique. *Opt. Express* **2003**, *11*, 3271.

(36) Forbes, A.; Dudley, A.; McLaren, M. Creation and detection of optical modes with spatial light modulators. *Adv. Opt. Photonics* **2016**, *8*, 200.

(37) Beijersbergen, M.; Allen, L.; van der Veen, H.; Woerdman, J. Astigmatic laser mode converters and transfer of orbital angular momentum. *Opt. Commun.* **1993**, *96*, 123−132.

(38) Fickler, R.; Campbell, G.; Buchler, B.; Lam, P. K.; Zeilinger, A. Quantum entanglement of angular momentum states with quantum numbers up to 10,010. *Proc. Natl. Acad. Sci. U. S. A.* **2016**, *113*, 13642−13647.

(39) Marrucci, L.; Manzo, C.; Paparo, D. Optical Spin-to-Orbital Angular Momentum Conversion in Inhomogeneous Anisotropic Media. *Phys. Rev. Lett.* **2006**, *96*, 163905.

(40) Biener, G.; Niv, A.; Kleiner, V.; Hasman, E. Formation of helical beams by use of Pancharatnam−Berry phase optical elements. *Opt. Lett.* **2002**, *27*, 1875.

(41) Yu, N.; Genevet, P.; Kats, M. A.; Aieta, F.; Tetienne, J.-P.; Capasso, F.; Gaburro, Z. Light Propagation with Phase Disconti-nuities: Generalized Laws of Reflection and Refraction. *Science* **2011**, *334*, 333−337.

(42) Karimi, E.; Schulz, S. A.; De Leon, I.; Qassim, H.; Upham, J.; Boyd, R. W. Generating optical orbital angular momentum at visible wavelengths using a plasmonic metasurface. *Light: Science & Applications* **2014**, *3*, e167.

(43) Chong, K. E.; Staude, I.; James, A.; Dominguez, J.; Liu, S.; Campione, S.; Subramania, G. S.; Luk, T. S.; Decker, M.; Neshev, D. N.; Brener, I.; Kivshar, Y. S. Polarization-Independent Silicon Metadevices for Efficient Optical Wavefront Control. *Nano Lett.* **2015**, *15*, 5369−5374.

(44) Devlin, R. C.; Ambrosio, A.; Wintz, D.; Oscurato, S. L.; Zhu, A. Y.; Khorasaninejad, M.; Oh, J.; Maddalena, P.; Capasso, F. Spin-to-orbital angular momentum conversion in dielectric metasurfaces. *Opt. Express* **2017**, *25*, 377.

(45) Devlin, R. C.; Ambrosio, A.; Rubin, N. A.; Mueller, J. P. B.; Capasso, F. Arbitrary spin-to−orbital angular momentum conversion of light. *Science* **2017**, *358*, 896−901.

(46) Seifert, T. S.; Tran, N. M.; Gueckstock, O.; Rouzegar, S. M.; Nadvornik, L.; Jaiswal, S.; Jakob, G.; Temnov, V. V.; Münzenberg, M.; Wolf, M.; Kläui, M.; Kampfrath, T. Terahertz spectroscopy for all-optical spintronic characterization of the spin-Hall-effect metals Pt, W and $Cu_{80}Ir_{20}$. *J. Phys. D: Appl. Phys.* **2018**, *51*, 364003.

(47) Tang, Y.; Cohen, A. E. Enhanced Enantioselectivity in Excitation of Chiral Molecules by Superchiral Light. *Science* **2011**, *332*, 333−336.

(48) Cameron, R. P.; Barnett, S. M.; Yao, A. M. Optical helicity, optical spin and related quantities in electromagnetic theory. *New J. Phys.* **2012**, *14*, 053050.

(49) Bliokh, K. Y.; Bekshaev, A. Y.; Nori, F. Optical Momentum, Spin, and Angular Momentum in Dispersive Media. *Phys. Rev. Lett.* **2017**, *119*, 073901.

(50) Padgett, M.; Allen, L. Light with a twist in its tail. *Contemp. Phys.* **2000**, *41*, 275−285.

(51) Fiebig, M. Revival of the magnetoelectric effect. *J. Phys. D: Appl. Phys.* **2005**, *38*, R123−R152.

(52) Lipkin, D. M. Existence of a New Conservation Law in Electromagnetic Theory. *J. Math. Phys.* **1964**, *5*, 696−700.

(53) Vázquez-Lozano, J. E.; Martínez, A. Optical Chirality in Dispersive and Lossy Media. *Phys. Rev. Lett.* **2018**, *121*, 043901.

(54) Shen, Y.; Wang, X.; Xie, Z.; Min, C.; Fu, X.; Liu, Q.; Gong, M.; Yuan, X. Optical vortices 30 years on: OAM manipulation from topological charge to multiple singularities. *Light: Science & Applications* **2019**, *8*, 90.

(55) Forbes, A.; de Oliveira, M.; Dennis, M. R. Structured light. *Nat. Photonics* **2021**, *15*, 253−262.

(56) Spektor, G.; Kilbane, D.; Mahro, A. K.; Frank, B.; Ristok, S.; Gal, L.; Kahl, P.; Podbiel, D.; Mathias, S.; Giessen, H.; Meyer zu Heringdorf, F.-J.; Orenstein, M.; Aeschlimann, M. Revealing the subfemtosecond dynamics of orbital angular momentum in nano-plasmonic vortices. *Science* **2017**, *355*, 1187−1191.

(57) Rego, L.; Dorney, K. M.; Brooks, N. J.; Nguyen, Q. L.; Liao, C.-T.; San Román, J.; Couch, D. E.; Liu, A.; Pisanty, E.; Lewenstein, M.; Plaja, L.; Kapteyn, H. C.; Murnane, M. M.; Hernández-García, C.

Generation of extreme-ultraviolet beams with time-varying orbital angular momentum. *Science* **2019**, *364*, No. eaaw9486.

(58) Yang, D.; Liang, J.; Zhou, C.; Sun, L.; Zheng, R.; Luo, S.; Wu, Y.; Qi, J. Powerful and Tunable THz Emitters Based on the Fe/Pt Magnetic Heterostructure. *Adv. Opt. Mater.* **2016**, *4*, 1944−1949.

(59) Jin, Z.; Zhang, S.; Zhu, W.; Li, Q.; Zhang, W.; Zhang, Z.; Lou, S.; Dai, Y.; Lin, X.; Ma, G.; Yao, J. Terahertz Radiation Modulated by Confinement of Picosecond Current Based on Patterned Ferromagnetic Heterostructures. *Phys. Status Solidi RRL* **2019**, *13*, 1900057.

📖 Recommended by ACS